Interdecadal Variations of the Thermohaline Circulation in a Coupled Ocean–Atmosphere Model

T. DELWORTH, S. MANABE, AND R. J. STOUFFER

Geophysical Fluid Dynamics Laboratory/NOAA, Princeton University, Princeton, New Jersey

(Manuscript received 5 September 1992, in final form 26 February 1993)

ABSTRACT

A fully coupled ocean–atmosphere model is shown to have irregular oscillations of the thermohaline circulation in the North Atlantic Ocean with a time scale of approximately 50 years. The irregular oscillation appears to be driven by density anomalies in the sinking region of the thermohaline circulation (approximately 52°N to 72°N) combined with much smaller density anomalies of opposite sign in the broad, rising region. The spatial pattern of sea surface temperature anomalies associated with this irregular oscillation bears an encouraging resemblance to a pattern of observed interdecadal variability in the North Atlantic. The anomalies of sea surface temperature induce model surface air temperature anomalies over the northern North Atlantic, Arctic, and northwestern Europe.

1. Introduction

Substantial variability in the North Atlantic Ocean occurs on time scales of decades, and is thought to be associated with fluctuations in the large-scale meridional overturning (Gordon et al. 1992). This meridional overturning consists of cold, saline water sinking at high latitudes of the North Atlantic and flowing equatorward at depth, upwelling throughout the world oceans, and returning as a northward flow of warm, salty water in the upper layers of the Atlantic Ocean. This overturning largely determines the oceanic component of the northward transport of heat from the tropics to higher latitudes, and thus plays an important role in maintaining the climate of the North Atlantic region (e.g., Manabe and Stouffer 1988). Fluctuations in the intensity of this overturning may have a significant effect on climate variations (Bjerknes 1964) of the North Atlantic and European regions. The presence of such interdecadal variability in the coupled ocean–atmosphere system may make the detection of anthropogenic climate change more difficult.

The incompleteness of the observational record makes it difficult to study variations in this overturning and associated processes based solely on the observational data. As a complementary approach, the output from a multicentury integration of a coupled ocean–atmosphere model is used to study the stability and variability of this meridional overturning [hereafter referred to as the thermohaline circulation (THC)]. The output from this model, developed at NOAA's Geophysical Fluid Dynamics Laboratory, forms the basis for the analyses presented here. The present study describes a result from our recent initiative to investigate the natural variability of the climate system through the use of coupled ocean–atmosphere models. It demonstrates that the state of the coupled ocean–atmosphere system can vary on time scales of decades in the absence of external forcings such as changing concentrations of greenhouse gases. Several previous modeling studies (Mikolajewicz and Maier-Reimer 1990; Weaver and Sarachik 1991; Weaver et al. 1991; Weaver et al. 1993) have used ocean-only models to study the variability and stability of the thermohaline circulation, in contrast to the fully coupled ocean–atmosphere model employed in the present investigation. Since the mechanisms for damping anomalies of temperature and controlling the freshwater flux at the ocean surface differ substantially between the two types of models, it is expected that the models might have different time scales for variations in the thermohaline circulation. While the quantitative results presented here may depend on the details of the model formulation and the physical parameterizations employed, it is hoped that the physical processes identified in this model study are robust and contribute to interdecadal variability in the North Atlantic.

2. Model description and experimental design

a. Coupled ocean–atmosphere model

The coupled ocean–atmosphere model used here was developed for the study of global warming. The structure and performance of the model were described by Stouffer et al. (1989), and in more detail by Manabe

Corresponding author address: Dr. Thomas L. Delworth, GFDL/NOAA, Princeton University, P.O. Box 308, Princeton, NJ 08542.

et al. (1991) and Manabe et al. (1992). The model consists of a general circulation model of the World Ocean coupled to a general circulation model of the atmosphere. Heat, water, and snow budgets at the continental surface are included. The model has global geography consistent with its computational resolution, and seasonally varying insolation.

In the atmospheric component of the model, dynamic computations are performed using the so-called spectral element method in which the distribution of a predicted variable is represented by a series of spherical harmonics (15 zonal waves and 15 associated Legendre functions) and grid values (Orszag 1970; Gordon and Stern 1982). There are nine unevenly spaced levels in the vertical. The effects of clouds, water vapor, carbon dioxide, and ozone are included in the calculation of solar and terrestrial radiation. Water vapor and precipitation are predicted in the model, but a constant mixing ratio of carbon dioxide and zonally uniform, seasonally varying distribution of ozone are prescribed. Overcast cloud is assumed whenever relative humidity exceeds a certain critical value. Otherwise, clear sky is predicted.

The basic structure of the oceanic component of the model is similar to the model described by Bryan and Lewis (1979). The finite-difference mesh used for the time integration of the primitive equations of motion has a spacing between grid points of 4.5° latitude and 3.7° longitude. It has 12 unevenly spaced levels for the finite differencing in the vertical direction. In addition to the horizontal and vertical background subgrid-scale mixing and convective overturning, the model has isopycnal mixing as discussed by Bryan (1987). The model predicts sea ice using a simple model developed by Bryan (1969).

The atmospheric and oceanic components interact with each other through the exchanges of heat, water (including ice), and momentum at their interface. The water/ice flux includes runoff from the continents to the oceans.

b. *Time integration*

When the time integration of a model starts from an initial condition that is not in equilibrium, the model climate usually undergoes a drift toward an equilibrium state. Such a drift contaminates the natural variability of the model climate that is the subject of the present study. Thus, it is highly desirable that the initial condition for the time integration be as close to equilibrium as possible.

Recently, Manabe and Stouffer (1988) have shown that a time integration of the original version of their model yielded an unrealistic equilibrium state, characterized by an exaggerated halocline in northern high latitudes and the absence of a significant thermohaline circulation in the North Atlantic. To offset this bias of the model, they adjusted the flux of water at the oceanic surface by an amount that varies geographically and seasonally but does not change from one year to the next during the integration of the model. With this adjustment, they obtained two stable equilibria with and without a thermohaline circulation of significant intensity in the Atlantic Ocean, depending on the initial condition chosen. Although the latter equilibrium resembles the state obtained earlier without the adjustment, the former equilibrium with the significant thermohaline circulation resembles the current condition in the Atlantic Ocean.

In the present study, the adjustment is performed for the fluxes of both water and heat at the oceanic surface. The seasonal and geographical distributions of the adjustment have no interannual variations and do not depend on the surface anomalies of temperature and salinity. Thus, the adjustments do not explicitly affect the feedback processes that reduce these anomalies. One should also note that, owing to the adjustments, the model fluctuates about a realistic equilibrium. The specific details on the determination of the initial quasi-equilibrium condition and the flux adjustment are described by Manabe et al. (1991) in section 3b of their paper.

Starting from an initial condition in quasi-equilibrium, the coupled model is time integrated over a period of 600 years. The mean rate of change in global-mean sea surface temperature of the model over this period is very small (~ 0.02°C century^{-1}).

3. Results

a. *Climatology and comparison to observed variability*

The climatological sea surface temperature (SST) and sea surface salinity (SSS) fields computed by the model are shown in Fig. 1 for the annual mean. Superimposed on each field are vectors indicating the direction and magnitude of the time-mean surface currents. Both the SST and SSS fields are in good agreement with observations (as would be expected when using the flux adjustments described previously). The structure of the mean temperature and salinity fields in the model plays a role in the variability results to be discussed below.

The spectra of model-generated and observed sea surface temperature in the northern North Atlantic are shown in Fig. 2. The thin, solid line represents the model SST spectrum from the grid point closest to the location of the observed SST, while the dashed line represents the spectrum from a model grid point farther to the north and west. A comparison of the spectrum of observed SST to the spectrum of model SST from the grid point closest to the observed SST reveals that although the model tends to underestimate the total variance, both spectra are indicative of red noise and resemble each other. One should note, however, that the present model does not resolve mesoscale eddies,

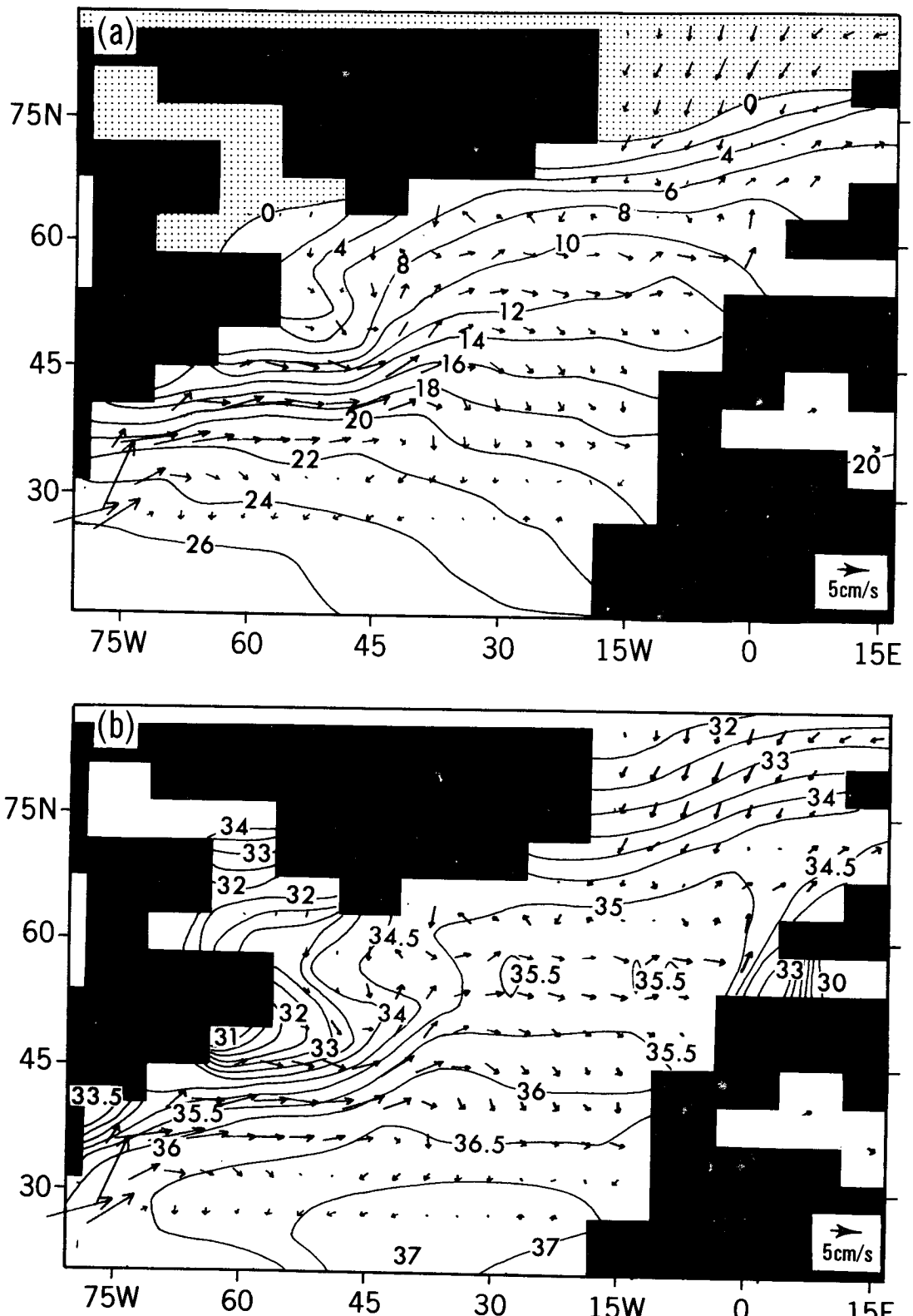

FIG. 1. (a) Map of long-term annual-mean sea surface temperature (°C), with long-term mean surface currents superimposed. For scaling, a vector indicating a current strength of 5 cm s^{-1} is indicated in the lower right-hand corner. (b) Map of long-term annual-mean sea surface salinity (practical salinity units), with long-term mean surface current vectors superimposed. For scaling, a vector indicating a current strength of 5 cm s^{-1} is indicated in the lower right-hand corner.

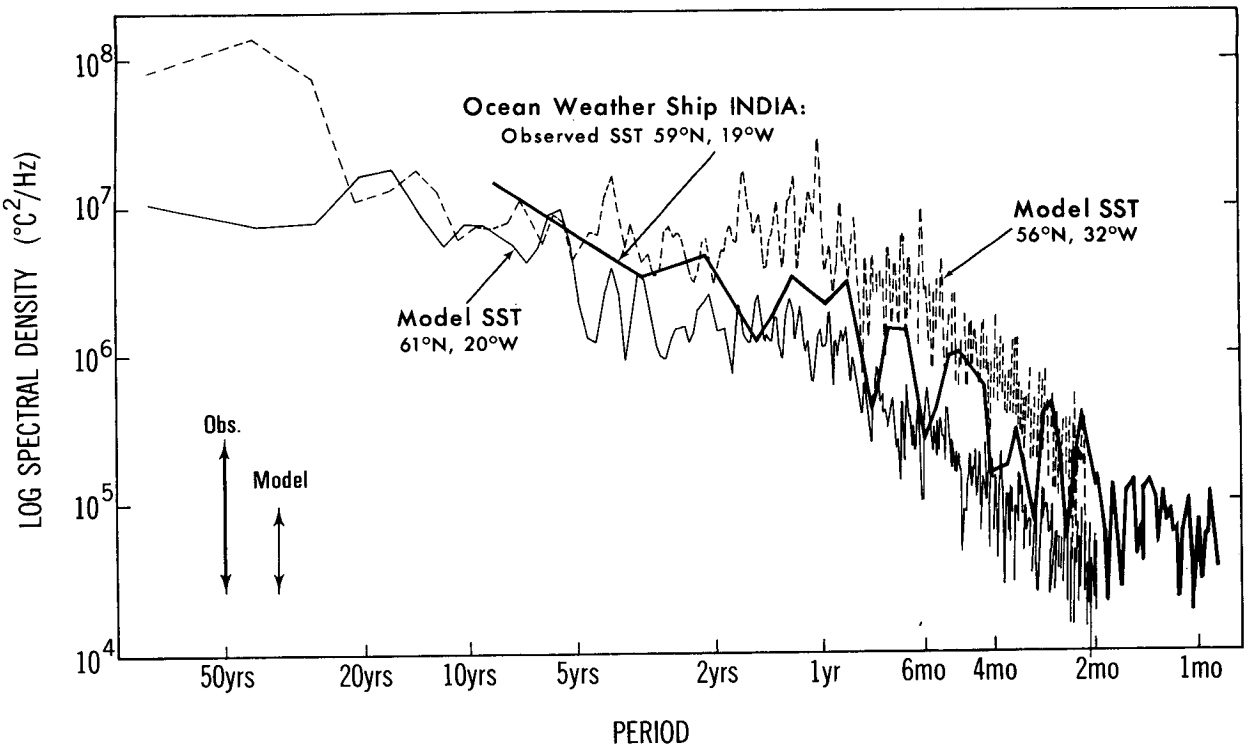

FIG. 2. Heavy, solid line: spectrum of sea-surface temperature from observed data (Ocean Weather Ship India station at 59°N, 19°W; spectrum constructed by Frankignoul and Hasselmann 1977). Light, solid line: spectrum of model sea surface temperature from grid point closest to 59°N, 19°W. Dashed line: spectrum of model sea surface temperature from grid point at 56°N, 32°W. The arrows in the lower left corner denote 95% confidence intervals about the spectra.

which may contribute significantly to the variability of sea surface temperature at seasonal to annual time scales. Note that the spectrum of model SST at 56°N, 32°W shows enhanced variability around the time scale of 50 years, which appears to be different from a red noise spectrum. As will be shown below, there are fluctuations in the intensity of the model THC at about this time scale that affect SST. This particular grid point is located in the region where SSTs are substantially affected by the THC fluctuations. In contrast, the region from which the other model spectrum is extracted is not substantially affected by the variations in the intensity of the THC (this will be shown in more detail below).

b. Meridional overturning index and variability

The streamfunction describing the meridional circulation in the Atlantic basin (200-year mean) is shown in Fig. 3. The circulation is in the direction of the arrows, and its magnitude is proportional to the gradient of the streamfunction. Note that the sinking region of the model THC is principally confined to the latitudinal belt from 52°N to 72°N (hereafter, the term "sinking region" refers to the region defined by this latitudinal belt, and extending from the western to the eastern boundaries of the basin).

In this study, the intensity of the THC in the North Atlantic is defined each year as the maximum value of the streamfunctions representing the annual-mean meridional circulation. A time series of this index, which represents the fluctuations in the intensity of the

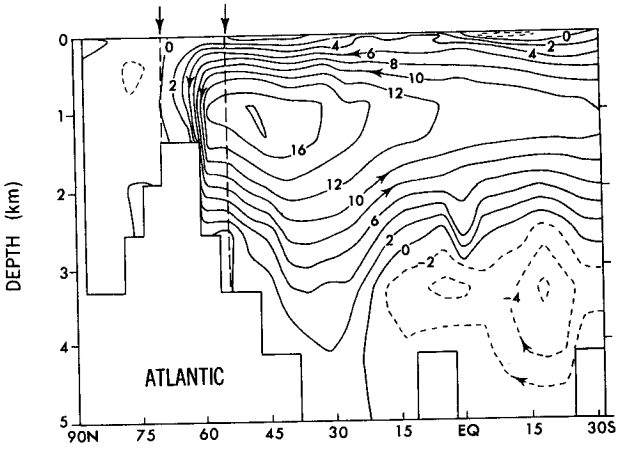

FIG. 3. Streamfunction of the meridional overturning in the Atlantic basin. Flow is in the direction of the arrows. Units are Sverdrups (10^6 m^3 s^{-1}). The dashed lines near 65°N latitude denote the sinking region as defined in the text.

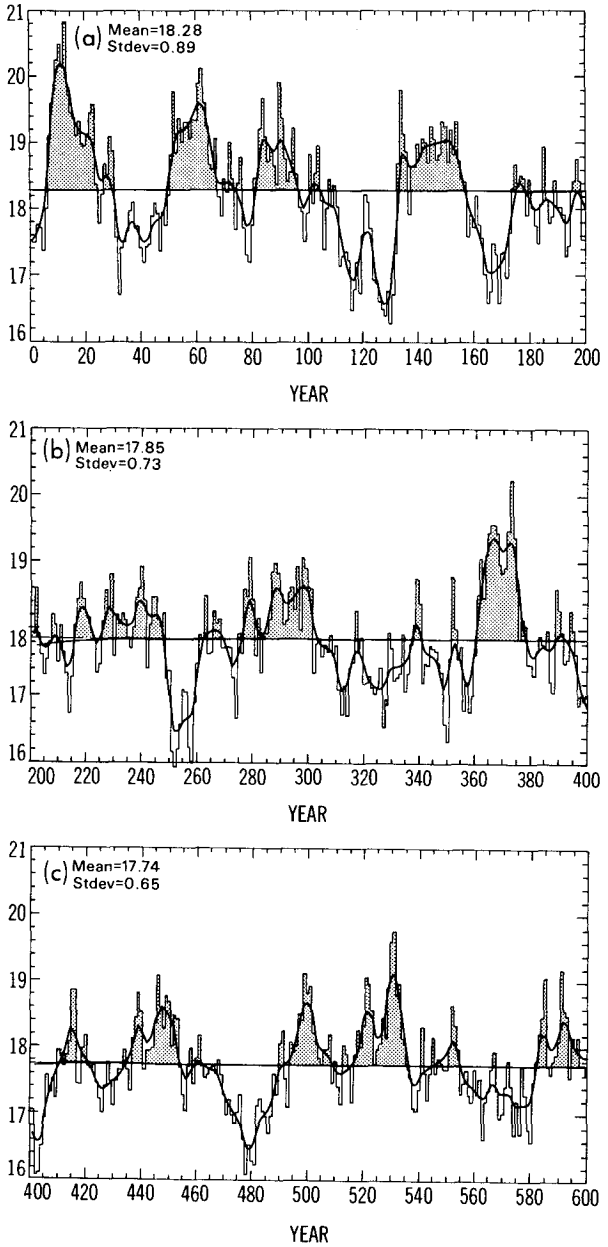

FIG. 4. Time series of the annual-mean intensity of the index of the meridional overturning in the North Atlantic. Units are Sverdrups (10^6 m^3 s^{-1}). Heavy, solid line is a smoothed time series computed by applying a 13-point binomial filter to the annual-mean data (approximately a 10-year low-pass filter). (a) Years 1–200, (b) years 201–400, (c) years 401–600.

annual-mean THC, is shown in Fig. 4. Visual inspection of this figure reveals substantial variability on interdecadal time scales, along with a quasi-oscillatory appearance to the time series. The fluctuations are present in all 600 years of the integration shown, although some of their characteristics vary with time. In particular, the time scale of the fluctuation appears somewhat longer for years 200 to 600 than in years 1 to 200. Spectral analysis of the time series from the first 200 years (Fig. 5) demonstrates enhanced variance in a fairly broad band around the 50-year time scale, while spectral analysis of years 200 to 600 (not shown) shows a broad peak around 60 years. Thus, these fluctuations have a very broad time scale.

c. *Sea surface temperature, salinity, and surface air temperature variations*

The spatial pattern of the anomalies of model sea surface temperature (SST) associated with fluctuations in the intensity of the THC is shown in Fig. 6a. These differences are computed by subtracting the mean of four decades with anomalously small values of the THC index from the mean of four decades with anomalously large values of the THC. The pattern of SST change bears encouraging resemblance to a pattern of observed interdecadal SST variation computed by Kushnir (1993), and shown in Fig. 6b [the observed SST pattern was computed as the difference between a period of anomalously warm SSTs in the North Atlantic (1950–1964) and a period with anomalously cold SSTs in the North Atlantic (1970–1984)]. The pattern of model sea surface salinity (SSS) changes (Fig. 6c) associated with fluctuations in the intensity of the THC resembles

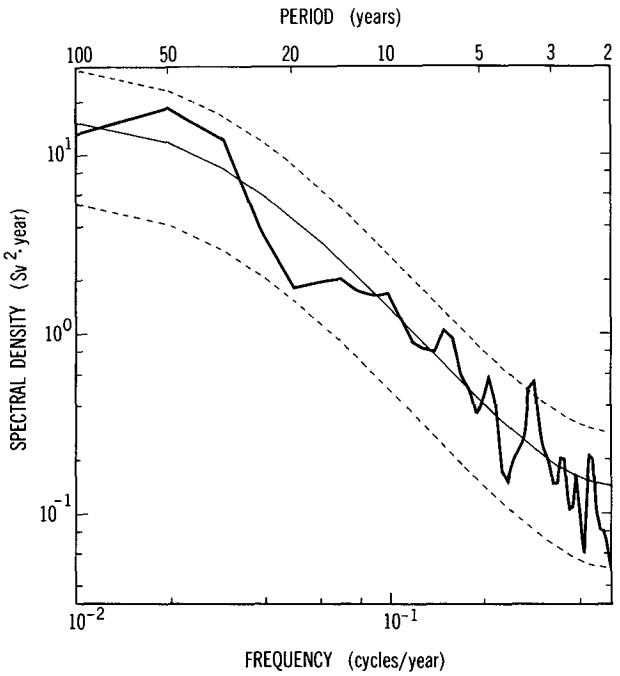

FIG. 5. Heavy, solid line denotes spectrum of the first 200 years of the thermohaline circulation index time series shown in Fig. 4. Thin, solid line denotes the least-squares best fit of a theoretical red noise spectrum to the spectrum of the thermohaline circulation. Dashed lines denote 95% confidence limits about the red noise spectrum. Note: the spectrum was computed by taking the Fourier transform of the autocovariance function, using a maximum of 50 lags and a Tukey window (Chatfield 1989, chapter 7).

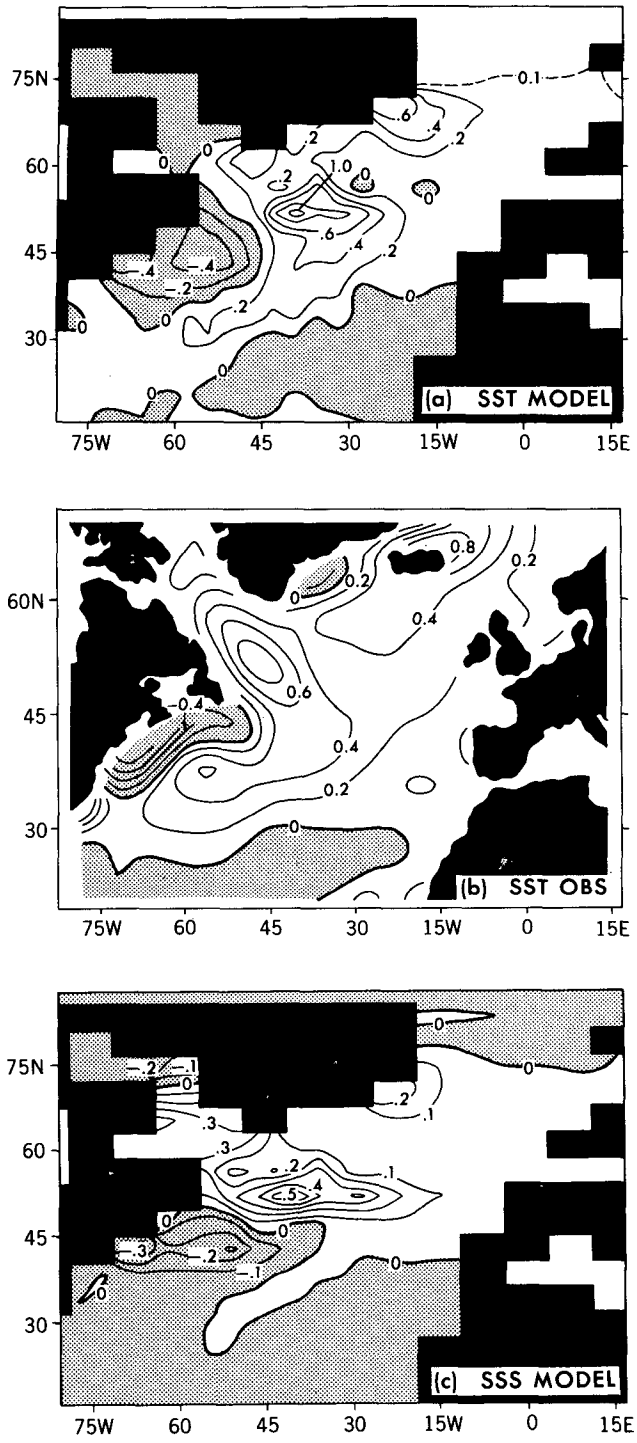

FIG. 6. (a) Differences in annual-mean model sea surface temperature between four decades with anomalously large THC index values and four decades with anomalously small THC index values. Units are degrees Celsius. Values less than zero are stippled. (b) Differences in observed sea surface temperature between the periods 1950–1964 (warm period) and 1970–1984 (cold period). Units are degrees Celsius. Values less than zero are stippled (adapted from Kushnir 1993). (c) Differences in annual-mean model sea surface salinity, computed in the same manner as (a). Units are practical salinity units.

the pattern of model SST changes. It should be noted that the pattern of model ocean temperature and salinity anomalies at 295 m depth (not shown) also resembles the observational results of Levitus (1989), in which differences in ocean temperature and salinity were computed between the five-year periods 1955–1959 and 1970–1974. As previously mentioned in discussing the SST spectra above, one of the model SST spectra shown in Fig. 2 is from a location with little change in SST associated with the THC fluctuations (near 59°N, 19°W), while the other spectrum is from a grid point in a region with larger SST changes associated with the THC fluctuations (56°N, 32°W).

The anomalies of surface air temperature in winter associated with fluctuations in the intensity of the THC are shown in Fig. 7. The geographical extent of the surface air temperature anomalies is not restricted to the North Atlantic, but encompasses large regions of Northern Europe and the Arctic. There is a polar amplification of the surface air temperature anomalies (this polar amplification does not occur in the summer—map not shown). This seasonal dependence in the high latitudes results partially from changes in sea ice thickness associated with the changes in the intensity of the THC. When the THC is anomalously strong, the enhanced transport of heat into high latitudes results in a reduction of mean sea ice cover (not shown), thereby permitting an enhanced heat flux from the ocean to the atmosphere during the winter months when the mean surface air temperatures are substantially less than those of the ocean at high latitudes. During the summer there is little or no heat flux from

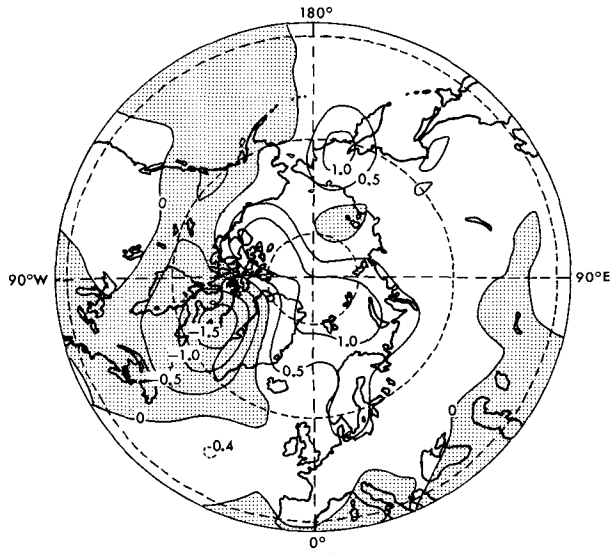

FIG. 7. Differences in surface air temperature computed in a similar manner as in Fig. 6a except that only data from Dec–Feb were used in the compositing. Values less than zero are stippled. A polar projection is used. Actual coastlines are used in the construction of this map in order to facilitate orientation. Units are degrees Celsius.

the model ocean to the atmosphere, and the surface air temperature remains near the freezing point in high latitudes. However, the enhanced surface absorption of summer insolation due to the reduced coverage of sea ice also contributes to the reduction of sea ice thickness and the increase of surface air temperature in winter as described above.

The above results highlight the potential importance of such fluctuations in the THC to climate over the North Atlantic, Europe, and the Arctic.

d. Mechanism

1) REGRESSION ANALYSES

It is anticipated that fluctuations in the intensity of the THC should be related to changes in the density, salinity, and temperature structure of the North Atlantic. These relations are investigated by computing linear regressions between the time series of temperature, salinity, and density at each grid point versus the THC. These regressions are computed at various lags in order to provide a three-dimensional picture of the evolution of the oceanic state as the THC fluctuates. Prior to the regression analyses, all time series were first detrended and filtered such that fluctuations with time scales less than approximately 10 years were effectively removed. The filtering uses the "finite impulse response" method as described by Bloomfield (1976). Note that regression analyses were also performed without filtering, and yielded phase relationships very similar to those described below. All of the analyses described below were performed on anomalies from the long-term annual mean using the first 200 years of the model integration. Thus, all terms in the analyses below should be regarded as anomalies, even if not stated explicitly.

The regressions of various quantities versus the THC intensity are shown in Fig. 8. For reference, the time series of the THC index is regressed against itself to provide some indication of the inherent time scale of these fluctuations. The minima in the regressions of the THC versus itself at lags of approximately −20 years and +20 years suggests an approximate time scale of 50 years. This time scale is actually quite broad, as discussed previously.

In order to provide a large-scale measure of conditions in the sinking region related to fluctuations in the THC, the regression coefficients were averaged vertically and horizontally over the sinking region of the North Atlantic, and are also plotted as a function of lag in years in Fig. 8. The regression coefficients plotted at lag −5 (+5) years indicate conditions 5 years prior (subsequent) to a maximum in the THC. The density time series leads the THC time series by a few years, suggesting that fluctuations in density in the sinking region induce the fluctuations in the THC. The density term is also decomposed into individual contributions from temperature and salinity anomalies. This figure

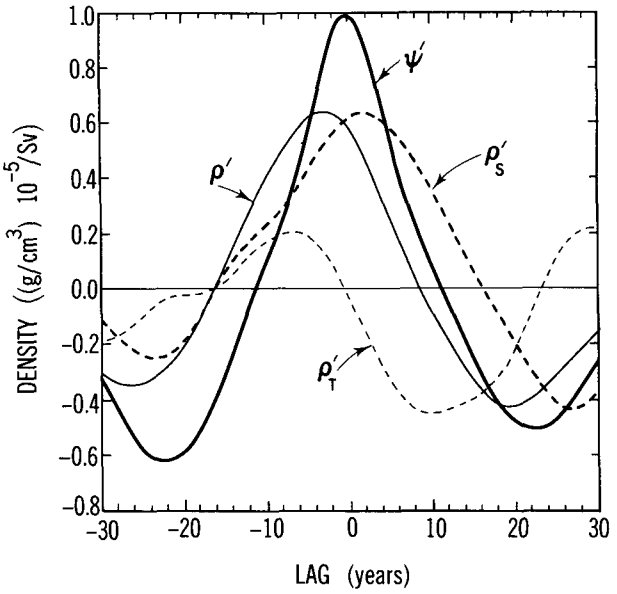

FIG. 8. Regression coefficients between various quantities and the time series of the THC index. The heavy, solid line (ψ') denotes the regression coefficients of the THC index with itself (thus representing a "typical" fluctuation). The thin, solid line (ρ') represents the regression coefficients between density and the THC index. The thick, dashed line (ρ'_S) denotes the regression coefficients for the density changes attributable solely to changes in salinity versus the THC index, while the thin, dashed line (ρ'_T) represents the regression coefficients for the density changes attributable solely to changes in temperature versus the THC index. The regression coefficients for ρ', ρ'_S, and ρ'_T were averaged vertically and horizontally over the sinking region.

indicates that density fluctuations attributable to salinity anomalies (ρ'_S) are almost in phase with, but slightly behind, the THC, whereas density fluctuations attributable to temperature anomalies (ρ'_T) precede the THC by almost 90° (assuming a time scale of approximately 40–50 years). Note that ρ'_T is inversely related to temperature, whereas ρ'_S is proportional to salinity. The sum of the effects of temperature and salinity anomalies results in a density time series that leads the THC by a few years, as indicated in this figure. The phase differences between ρ'_S and ρ'_T shown in Fig. 8 are important to the oscillatory nature of the fluctuations, as will be discussed later.

The phase relation between temperature and the THC varies with depth. Shown in Fig. 9a are the regressions of sea surface temperature (SST) versus the THC, as well as sea surface salinity (SSS) versus the THC. The SST and SSS regressions shown in Fig. 9a were averaged over a region near the southern boundary of the sinking region (50°N–59°N, 43°W–25°W), where anomalies of SST and SSS associated with the THC are largest (see Figs. 6a and 6c). Shown in Fig. 9b are the regressions of temperature and salinity (averaged vertically and horizontally over the entire sinking region) versus the THC. Note that SST is approx-

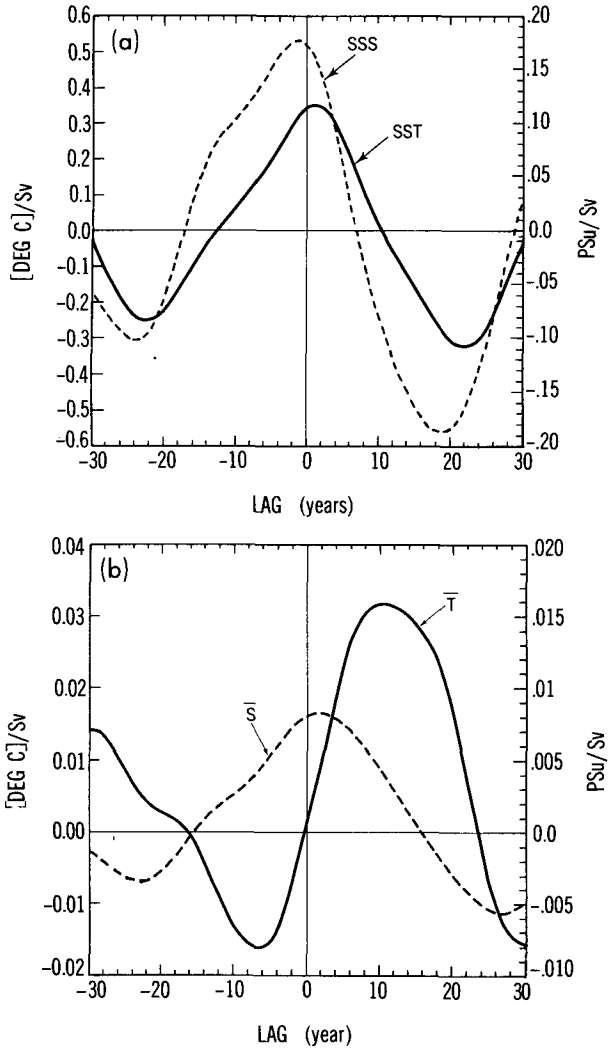

FIG. 9. (a) Regression coefficients of sea surface temperature (solid line: SST) and sea surface salinity (dashed line: SSS) versus the THC plotted as a function of lag in years. Units are °C Sv^{-1} for temperature and (practical salinity units Sv^{-1}) for salinity. (b) Regression coefficients between vertically averaged temperature (solid line: $\bar{T}$) and salinity (dashed line: $\bar{S}$) versus the THC. Units are °C Sv^{-1} for temperature, and (practical salinity units Sv^{-1}) for salinity.

imately in phase with the THC, whereas vertically averaged temperature lags the THC by approximately 10 years. In contrast, SSS and vertically averaged salinity are both approximately in phase with the THC. However, SSS slightly leads the THC (this may be significant in terms of the near-surface density anomalies discussed below).

The importance of density anomalies in the sinking region is underscored by Fig. 10, in which the zonal means across the Atlantic basin of the linear regression coefficients between density and the THC are shown. The regression coefficients are computed at lag -3 years, indicating that the density values at year $(n-3)$ are related to values of the THC index at year n. This lag corresponds to the phase with the maximum vertically averaged density perturbation in the sinking region (see Fig. 8). This figure indicates that, in the sinking region, positive density anomalies extend very deep. The density anomalies are particularly large in the near-surface layer, thereby altering the vertical stability and influencing the rate of convective exchange between the near-surface and deeper layers of the ocean. Note also the smaller negative density anomalies to the south of the sinking region. It is clear that there are changes in both the vertical and meridional density gradients associated with fluctuations in the THC intensity.

The zonal means of the regressions between temperature and salinity versus the THC are shown in Figs. 11a and 11b, respectively. Note that the regression for temperature was computed for lag +10 years, while the regression for salinity was computed for lag +3 years. These lags correspond to the times with maximum vertically averaged temperature and salinity, respectively (see Fig. 8). Note that the salinity anomalies penetrate quite deeply in the sinking region (corresponding to the density anomalies in Fig. 10). Further, note that the latitude at which temperature anomalies are at a maximum is distinctly south of the latitude at which salinity anomalies are at a maximum.

A geographical perspective on the density variations related to fluctuations in the THC index is shown in Fig. 12, in which the regressions between surface density and the THC at lag 0 are shown. Note that when the intensity of the THC is at a maximum, positive density anomalies occur primarily in the western North Atlantic and the Labrador Sea. While there are some positive density anomalies in the Greenland and Nor-

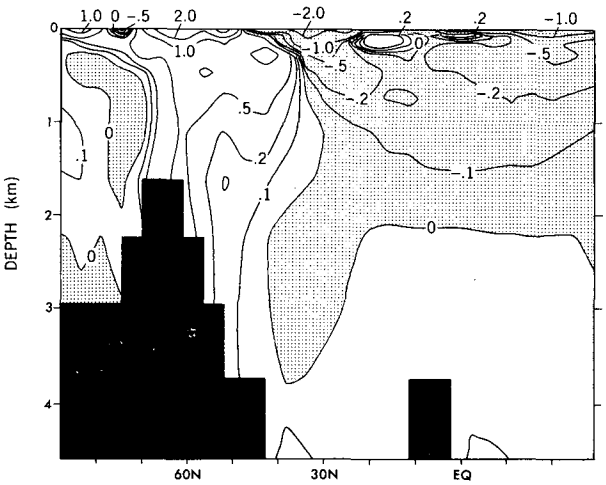

FIG. 10. Latitude by depth cross section in the Atlantic basin of the zonal mean of the regression coefficients between the time series of density and the THC computed at lag -3 years. Units are (10^{-5} g cm^{-3} Sv^{-1}). Values less than zero are stippled. This cross section can be interpreted as the anomalous density structure three years prior to a maximum in the THC.

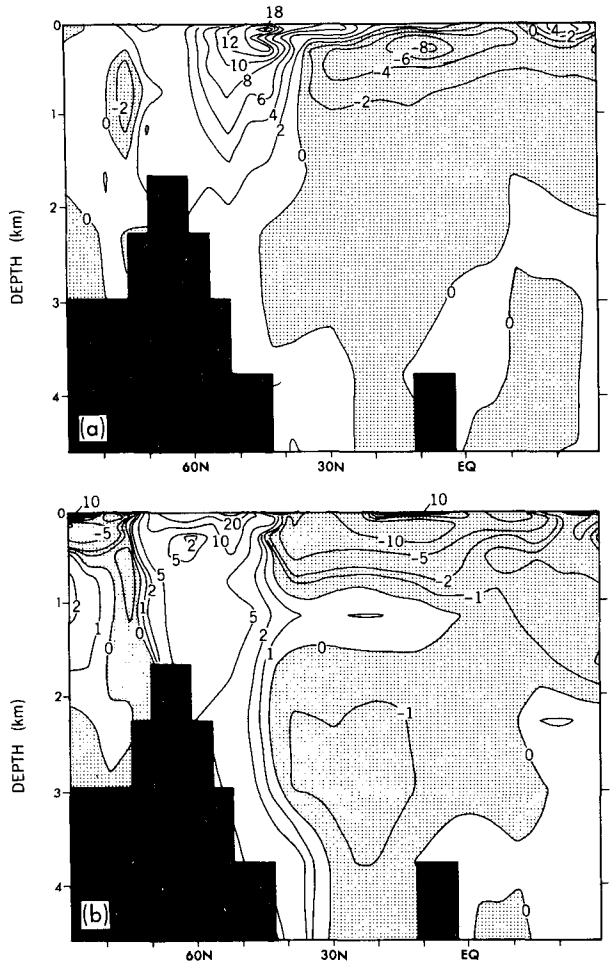

FIG. 11. (a) Latitude by depth cross section in the Atlantic basin of the zonal mean of the regression coefficients between the time series of temperature and the THC computed at lag + 10 years. Units are (10^{-2} °C Sv^{-1}). Values less than zero are stippled. This cross section can be interpreted as the anomaly temperature structure ten years after a maximum in the THC. (b) Same as (a), but for salinity at lag + 2 years. Units are (10^{-3} psu Sv^{-1}). Values less than zero are stippled. This cross section can be interpreted as the anomalous salinity structure two years after a maximum in the THC. A contour value of 10 indicates a zonal mean anomaly of 10^{-2} psu for a 1 Sv change in THC intensity.

wegian seas, the density perturbations are primarily confined to the western North Atlantic. A decomposition of the near-surface density anomalies in the Labrador Sea into temperature and salinity-induced components (not shown) has demonstrated that the near-surface density anomalies are strongly influenced by salinity anomalies north of approximately 55°N, but are primarily determined by temperature anomalies further equatorward.

2) BUDGET ANALYSES

It is clear that density in the sinking region is a forerunner of the intensity of the THC. Thus, diagnosing the variations of density in the sinking region—and how they are generated—is a critical aspect of diagnosing the mechanism of these fluctuations. Since the density variations are determined by anomalies of both temperature and salinity, we must examine the variations of both these quantities, as well as the processes by which the temperature and salinity anomalies are generated.

The phase relationships of heat and salt averaged vertically and horizontally over the sinking region will be interpreted within the following simplified framework:

$$\frac{\partial}{\partial t}(C_pT, S) = \text{net horizontal transport of (heat, } S\text{) into the sinking region + vertical flux of (heat, fresh water) through the ocean surface} \quad (1)$$

where (T, S) refers to temperature (T) or salinity (S) averaged vertically and horizontally over the sinking region, and C_p is the heat capacity. [The details of the computation of the vertical fluxes and horizontal transports may be found in the Appendix. Note that in Eq. (1) the contributions from horizontal diffusion and the melting/freezing of sea ice are neglected.] Within this framework, the time series of (T, S) will lag approximately 90° behind the sum of the horizontal transport and the surface flux [i.e., right-hand side of (1)]. Evaluating the net horizontal transports of heat and salt into the sinking region, as well as the surface fluxes of heat and fresh water, will assist in determining the physical processes controlling the phase dependence of temperature and salinity in the sinking region. It will be shown that the phases of the net *horizontal* transports of heat and salt into the sinking region largely determine the phases of vertically averaged temperature and salinity in the sinking region.

In order to evaluate the terms in (1), a budget volume was defined as shown schematically in Fig. 13. The budget volume encompasses most of the sinking

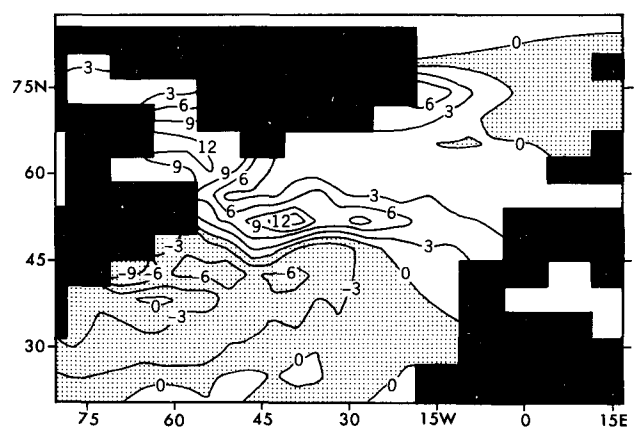

FIG. 12. Regression coefficients between surface density and the THC intensity for lag + 0 years. Units are 10^{-5} g cm^{-3} Sv^{-1}.

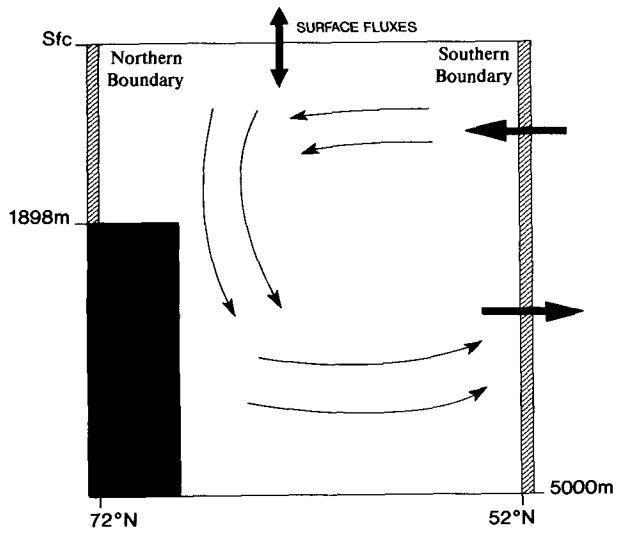

FIG. 13. Schematic cross section of the sinking region. For the budget computations, horizontal transports of heat and salt (fresh water) were computed through the northern and southern boundaries. The horizontal arrows through the southern boundary denote the mean northward flow in the upper layers, and the mean southward flow at lower layers. The arrows in the interior of the sinking region represent in a schematic fashion the zonal-mean flow.

region of the model THC, extending from 52°N to 72°N across the entire longitudinal extent of the North Atlantic. Monthly mean values were used to compute transports of heat and salt into the sinking region through both the northern and southern boundaries of the sinking region, as well as the surface fluxes of heat and fresh water across the air–sea interface. The regression coefficients between the horizontal transports and the THC, as well as between the surface fluxes and the THC, are shown in Fig. 14 for the heat budget, and Fig. 15 for the salt budget. The horizontal transports were normalized such that they have the same units as the surface fluxes, and are thus directly comparable. Positive values indicate a net anomalous transport/flux of heat or salt *into* the sinking region. For example, in the climatological mean there is a net heat flux from the ocean to the atmosphere. Positive values of the regression coefficients for the surface heat flux in Fig. 14 indicate that the flux of heat from the ocean to the atmosphere is weaker than normal, thereby removing less heat than normal from the ocean so that the surface heat flux is acting as an anomalous input of heat to the ocean in the sinking region. Note that the horizontal transports of both heat and salt into the sinking region through the northern boundary are relatively small compared to the transport through the southern boundary. Also note that variations in the surface water flux are relatively small (in contrast to variations in the surface heat flux).

For the heat balance, Fig. 14 demonstrates that the sum of the variations in the surface fluxes and the horizontal transport into the sinking region from the south is approximately in phase with the THC. Therefore, by the above discussion of (1), the temporal variations of vertically averaged temperature lag substantially (approximately 10 years) behind the THC. The maximum vertically averaged temperature (see Fig. 9) occurs just after the sum of the net horizontal transport and the surface flux crosses the zero line.

Averaged over the sinking region, the variations in the surface heat flux are comparable in magnitude to the variations in the horizontal heat transport. To zeroth order, the anomalous surface heat flux is opposite in sign to the anomalous horizontal transport through the southern boundary. There is, however, a small phase difference between the surface heat flux and the horizontal heat transport through the southern boundary, such that there is a period when both the surface flux and the horizontal transport have the same sign (at approximately lag +5). At this time, both terms are acting to add heat to the sinking region. The net effect is that the total anomalous heat supply to the sinking region is positive for longer than would be the case if there were only an anomalous horizontal heat transport. As can be seen from Fig. 14, the result of this phase difference is that the maximum in the total anomalous heating of the water column (sum of horizontal transport and surface flux) occurs several years after the maximum in the horizontal heat transport through the southern boundary. This phase difference

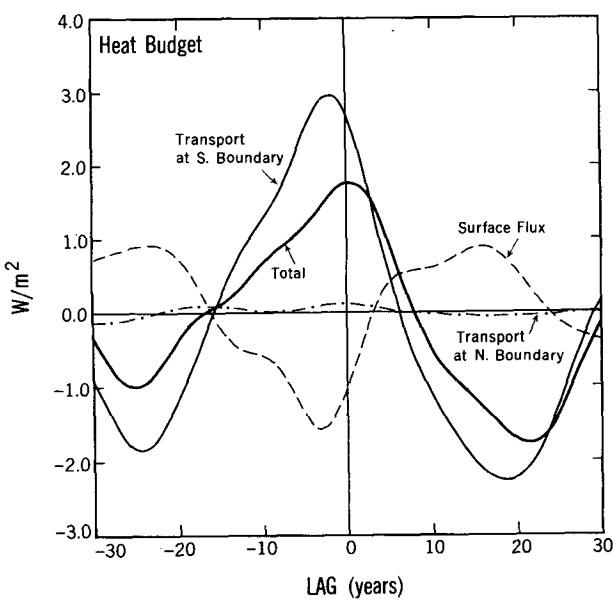

FIG. 14. Regression coefficients of various heat budget terms versus the THC, plotted as a function of lag in years. For all terms, values greater than zero imply a net anomalous heat flux into the sinking region. Units are W m^{-2}. Thin, solid line: net heat transport through the southern boundary. Dash-dotted line: net heat transport through the northern boundary. Dashed line: heat flux through the air–sea interface. Thick, solid line: sum of the other three terms.

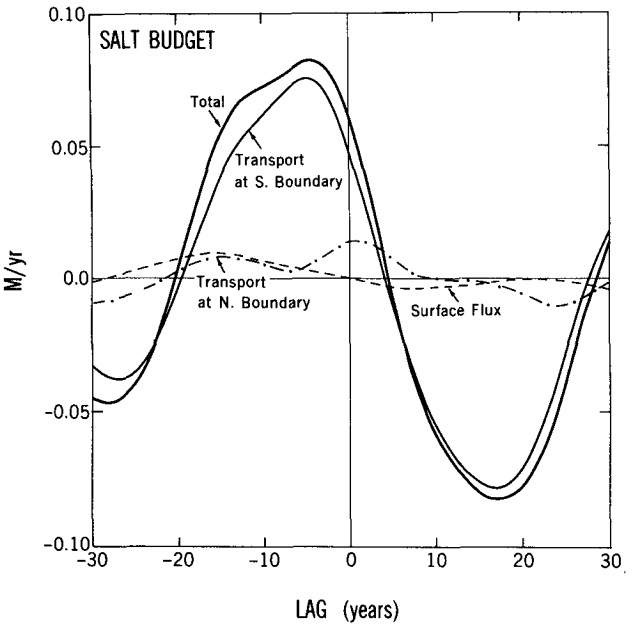

FIG. 15. Regression coefficients of various salt (fresh water) budget terms versus the THC, plotted as a function of lag in years. Units are M yr^{-1}. For all terms, values greater than zero imply a net salt flux into the sinking region (i.e., a removal of fresh water from the volume). Thin, solid line: net salt transport through the southern boundary. Dash-dotted line: net salt transport through the northern boundary. Dashed line: salt (fresh water) flux through the air–sea interface (in this context, a positive salt flux into the volume represents a net anomalous removal of fresh water from the volume, via excess evaporation or other processes). Thick solid line: sum of the other three terms.

between the maximum heat transport and the maximum in the total heating is attributable to the phase of the surface heat flux, and causes the maximum temperature to occur later than it would have based solely on the horizontal heat transport. Additional analyses (not shown) have revealed that the phase of the surface heat flux is closely related to anomalies in the near-surface wind intensity. This relation may represent an atmospheric role in this fluctuation.

In marked contrast to vertically averaged temperature, vertically averaged salinity is approximately in phase with the THC (see Fig. 9). This phase difference between salinity and temperature is attributable not only to the absence of substantial contributions from the surface water flux variations, but also to the earlier phase of the salt transport from the south relative to the heat transport (compare the transports in Figs. 14 and 15). The phase of vertically averaged salinity is largely a reflection of the phase of the net horizontal salt transport.

The fact that vertically averaged salinity in the sinking region is approximately in phase with the THC can be deduced from the salt budget regressions in Fig. 15, but the question remains as to why the salt transport precedes the heat transport. Part of the explanation lies in the differing vertical penetration of heat and salt anomalies in the sinking region, as shown previously by the cross sections of the regression coefficients of temperature and salinity in Fig. 11. Note that substantial anomalies of salt penetrate to the deepest ocean layers, whereas temperature anomalies do not penetrate as well because the near-surface density anomalies induced by the temperature anomalies are relatively small (note that the thermal expansion coefficient of water at standard pressure becomes quite small as the water temperature approaches the freezing point). The meridional transport of salt into the sinking region from the south is proportional to the salinity difference between the upper and lower layers at the southern boundary of the sinking region (since the flow in the upper layer is generally *into* the sinking region, and the flow at depth is generally *out of* the sinking region). The deep vertical penetration of salinity anomalies, coupled with the southward flow at depth, implies that the *southward* transport of salt at depth is enhanced when positive salt anomalies, first present in the upper layers of the sinking region, penetrate to the deeper layers. This southward flow at depth removes salt from the sinking region, thereby reducing the net northward transport of salt into the sinking region and causing the maximum in the net northward salinity transport to occur before the maximum net northward heat transport, as shown schematically in Fig. 16. Note in

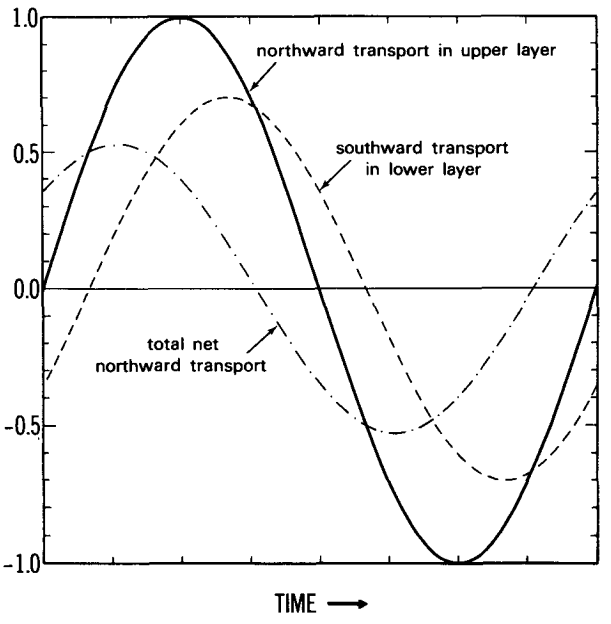

FIG. 16. Schematic illustration of the relative phases of the salt transport through the southern boundary of the sinking region (in relation to the intensity of the THC). The thick, solid line depicts the northward transport in the upper layer, the dashed line depicts the southward transport in the lower layer, and the dot-dashed line depicts the net northward transport (upper northward transport minus lower southward transport). Units are arbitrary.

this figure that the maximum in the *net* northward transport *precedes* the maximum transport in the upper layer. The net northward transport is maximum when there is substantial northward transport in the upper layer, with little southward transport at depth. As the southward transport at depth increases (i.e., when salt anomalies penetrate to the deeper layers), the net northward salt transport decreases.

Since temperature anomalies do not penetrate as deeply as salinity anomalies (see Fig. 11), the phase of the net heat transport is closer to the phase of the northward heat transport in the upper layer. Therefore, the phase of the net salt transport precedes the phase of the net heat transport. This phase difference is partially responsible for the phase difference between vertically averaged temperature and salinity shown in Fig. 9.

It should be noted that while anomalies in the surface water flux have the proper phase to increase salinity (and thus density) in the sinking region as the THC intensifies (i.e., approximately lags −20 years to 0 years), the magnitude of the surface water flux variations is much smaller than the variations in the horizontal transports. The net horizontal transport is the primary determinant of the vertically averaged salt content. However, the possibility remains that variations in the surface water flux may play a role in the THC fluctuations by altering the vertical stability of the water column.

It is critical to the fluctuations that the salt transport substantially precedes the THC. This condition is important in generating density anomalies in the sinking region that precede the THC. This phase relationship is at first perplexing, however. How can the salt transport precede the THC, if variations in the THC are responsible for variations in the salt transport? To address this question, the net northward heat and salt transports by the transient flow are decomposed into "meridional overturning" and "gyre" components as follows:

$$v'q = [v']q + (v')^*q, \qquad (2)$$

where ( )′ denotes a deviation from the time mean, [ ] denotes a zonal mean across the Atlantic basin, ( )* denotes the deviation from the zonal mean across the Atlantic, v is meridional velocity, and q is either temperature or salinity. (The term "gyre" here is purely mathematical, and does not imply any connection with the wind-driven circulation.) The first term on the right-hand side (rhs) of (2) denotes the portion of the anomalous transport accomplished by meridional overturning, and the second term on the rhs denotes the portion of the anomalous transport accomplished by the recirculating horizontal gyre component. The regressions of these terms for the heat and salt transports through the southern boundary versus the THC are shown in Fig. 17. It is clear that the horizontal gyre

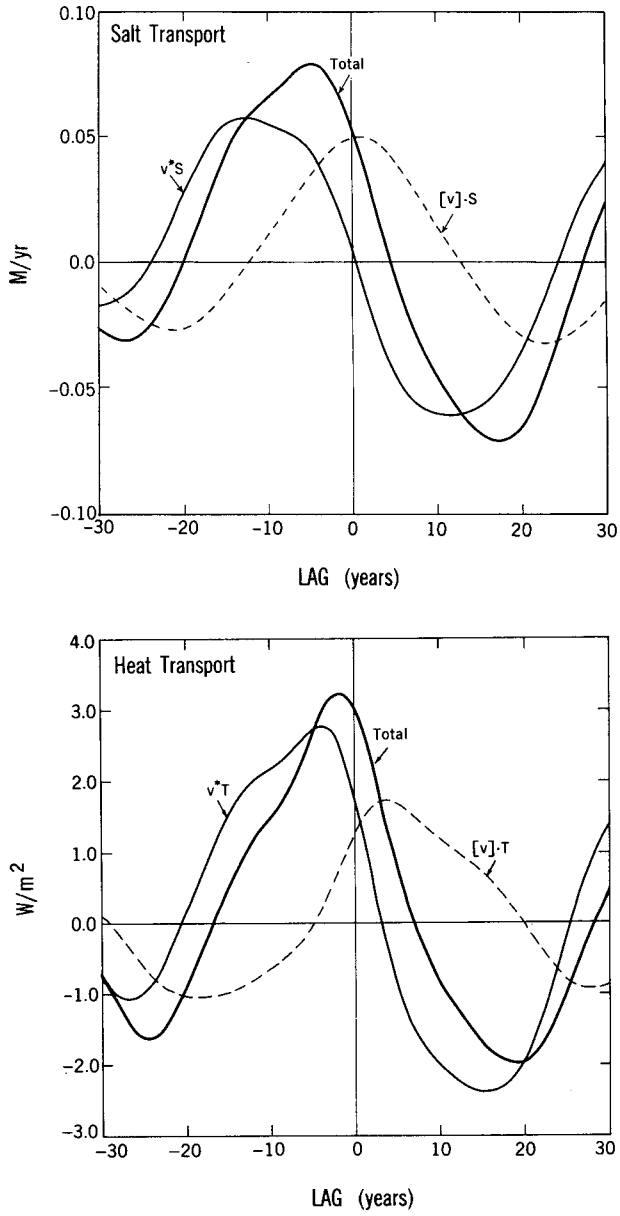

FIG. 17. Regression coefficients of the decomposition of the heat and salt transports through the southern boundary into the terms as defined in Eq. (2), and using the notation defined in the text; s is salinity, T is temperature, v is meridional velocity. (Top) Salt transport. Thin solid line denotes v^*s; dashed line denotes $[v]s$; thick solid line denotes the sum of the two components. (Bottom) Heat transport. Thin solid line denotes v^*T; dashed line denotes $[v]T$; thick solid line denotes the sum of the two components.

component of the salt transport is responsible for the phase of the total horizontal salinity transport preceding the THC. In fact, the gyre transport is more than 90° ahead of the transport by the meridional overturning, which is approximately in phase with the THC.

This gyre circulation can be seen in Fig. 18, which

shows the regressions of currents at 170 m depth versus the THC for lags −10, 0, and +10 years (the spatial pattern of the regressions between the currents and the THC is approximately uniform throughout the top 1 km). A comparison with Fig. 17 indicates that the net gyre salt transport is maximum and minimum around lags −12 and +10, respectively. The currents at these lags clearly demonstrate the gyre component of the circulation. By contrast, the meridional overturning (i.e., zonal mean of the meridional flow) is maximum at lag 0. This can also be clearly seen from the current vectors in Fig. 18 (i.e.,

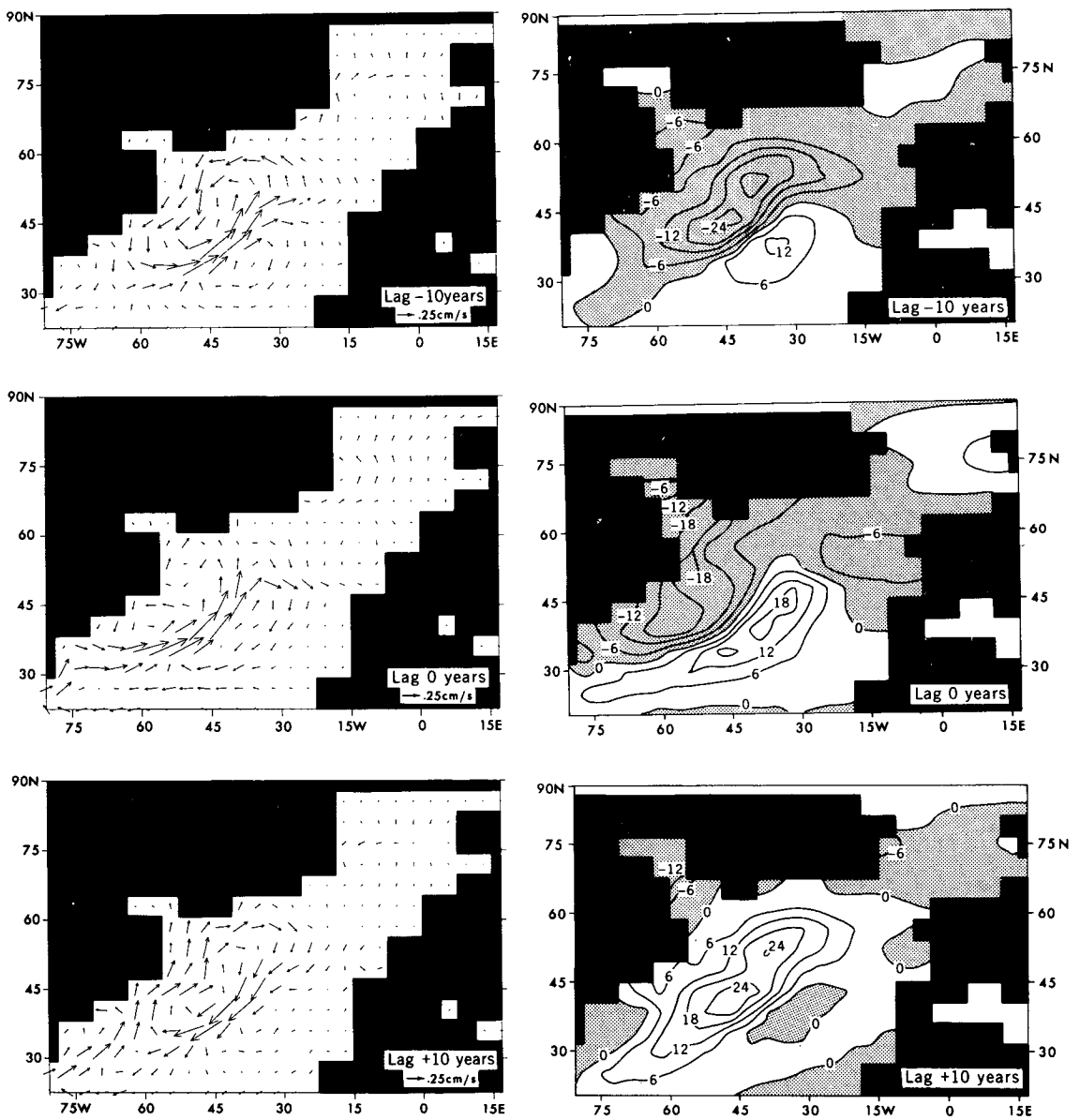

FIG. 18. Regression coefficients between various quantities and the THC intensity. The top row depicts regressions for lag − 10 years, the middle row depicts regressions for lag 0 years, the bottom row depicts regressions for lag + 10 years. Left column: regressions for currents at 170 m depth in the ocean versus the intensity of the THC. At each grid point, regression coefficients were computed between the u (zonal) component of the current and the THC, as well as between the v (meridional) component of the current and the THC. These regression coefficients are then plotted at each grid point in vector form, such that the length of the arrow in the zonal (meridional) direction denotes the magnitude of the regression coefficients between the zonal (meridional) component of the current and the THC. Right column: regressions between anomalies of dynamic topography and the THC. Dynamic topography was computed from the surface to 915 dbar. Values less than zero are stippled. Units are 10^2 cm^2 s^{-2}.

the zonal mean across the Atlantic of the meridional velocity is nonzero).

The phase of the gyre transports can be inferred by comparing Fig. 18 with the time-mean temperature and salinity fields shown in Fig. 1. At lag −10 years, the gyre circulation is transporting northward the warmer, more saline water in the eastern North Atlantic, while transporting southward the colder, fresher water in the far western North Atlantic. (Note that these transports are computed at 52°N—see Fig. 1 for the mean temperature and salinity fields at the surface.) The result is an anomalously strong northward heat and salt transport into the sinking region. The reverse situation occurs at lag +10 years. Note also that for salinity the westward flow near 60°N associated with the gyre circulation at lag −10 years is transporting the relatively saline water in the eastern North Atlantic toward the region of the Labrador Sea, thereby increasing the salinity and density in this region.

The SST and SSS anomaly patterns in Fig. 6 may be interpreted as the result of the advection by the gyre circulation between lags −10 years and +0 years. The warm and cold anomalies in SST in Fig. 6a are coincident with the enhanced northward and southward currents shown in Fig. 18 for lag −10 years. Thus, the phase of the gyre circulations contributes to the SSTs being in phase with the THC. This process is in addition to the damping of SST anomalies through the surface heat flux. The warming off the southeast coast of Greenland is consistent with the flow around a weak anticyclonic gyre between Greenland and northwestern Europe at lag −10 years.

The transport of heat and salt by the gyre circulation is largest in the near-surface layers (since both the currents and the gradients of temperature and salinity are largest in the near-surface layers). As a result, the anomalous freshwater transport into the sinking region by the gyre circulation affects the salinity of the near-surface layers to a greater degree than the deeper layers. These changes in near-surface salinity alter the near-surface density, and thus the vertical density gradient. Depending on the phase of the fluctuation, the maximum gyre transport in the near-surface layers can provide either an effective freshwater cap to inhibit convection, or an anomalously dense near-surface layer to enhance convection. Thus, the freshwater transport by the gyre circulation not only changes the mean density of the entire water column in the sinking region, but also changes the vertical density gradient.

The gyre circulations, which are crucial to the phase of the salt transport, are related geostrophically to density perturbations throughout the top 1 km. In order to illustrate this, time series of dynamic topography (height) anomalies were computed from the surface to 915 dbar. Regressions were then computed between the dynamic topography anomalies and the THC, and are shown in Fig. 18 at lags −10, 0, and +10 years. Note that positive (negative) density anomalies are consistent with negative (positive) anomalies of dynamic topography. The horizontal gradient of the dynamic topography anomalies indicates the vertical shear of the geostrophic currents between 915 dbar and the surface, and is a good indicator of the anomalous flow throughout the top 1 km of the model ocean. This can be verified by comparing the left column of Fig. 18 to the right column. The anomalous surface currents are clearly related geostrophically to the anomalies in dynamic topography.

The dynamic topography anomalies shown in Fig. 18 can be decomposed into temperature- and salinity-induced components, as shown in Fig. 19. The salinity-(temperature) induced component of the dynamic topography anomalies denotes the anomaly in dynamic topography attributable exclusively to salinity (temperature) changes. (Note that this decomposition is only approximate due to both the nonlinearity of the equations of state of saltwater and the inverse relation between density and dynamic topography; nevertheless, the small perturbations of temperature and salinity associated with the THC fluctuations permit this linear decomposition. Maximum errors in performing this decomposition were quite small.) It is clear that the total anomalies of dynamic topography—and thus the changes in circulation—are dominated by temperature anomalies in the region where the gyre circulation exists (i.e., between approximately 30°N and 55°N). Cyclonic circulations surround the negative dynamic topography anomalies (cold water), whereas anticyclonic circulations surround the positive dynamic topography anomalies (warm water). Note also that in the region of the Labrador Sea, salinity-induced perturbations of dynamic topography are substantial.

The dynamic topography anomalies at lag 0 shown in Fig. 18 are consistent with an east–west pressure gradient that is necessary to geostrophically support the anomalous northward flow in the upper layer when the THC is strong. As seen in Fig. 19, temperature anomalies are primarily responsible for this zonal gradient of dynamic topography from approximately 20°N to 55°N. North of approximately 55°N, the influence of salinity anomalies on density anomalies is substantial in the near-surface layers of the Labrador Sea and western North Atlantic. The relative importance of salinity or temperature anomalies on the density anomalies (and thus on dynamic topography anomalies) is related to the dependence of the thermal expansion coefficient of seawater on temperature. In warmer regions, thermal effects tend to dominate, while in colder regions salinity effects are more substantial. Thus, the combination of temperature and salinity-induced density anomalies generates the zonal gradient of dynamic topography necessary for the anomalous northward flow in the upper layer when the THC is strong.

There is a very close relationship between the gyre circulation and density in the sinking region, and hence

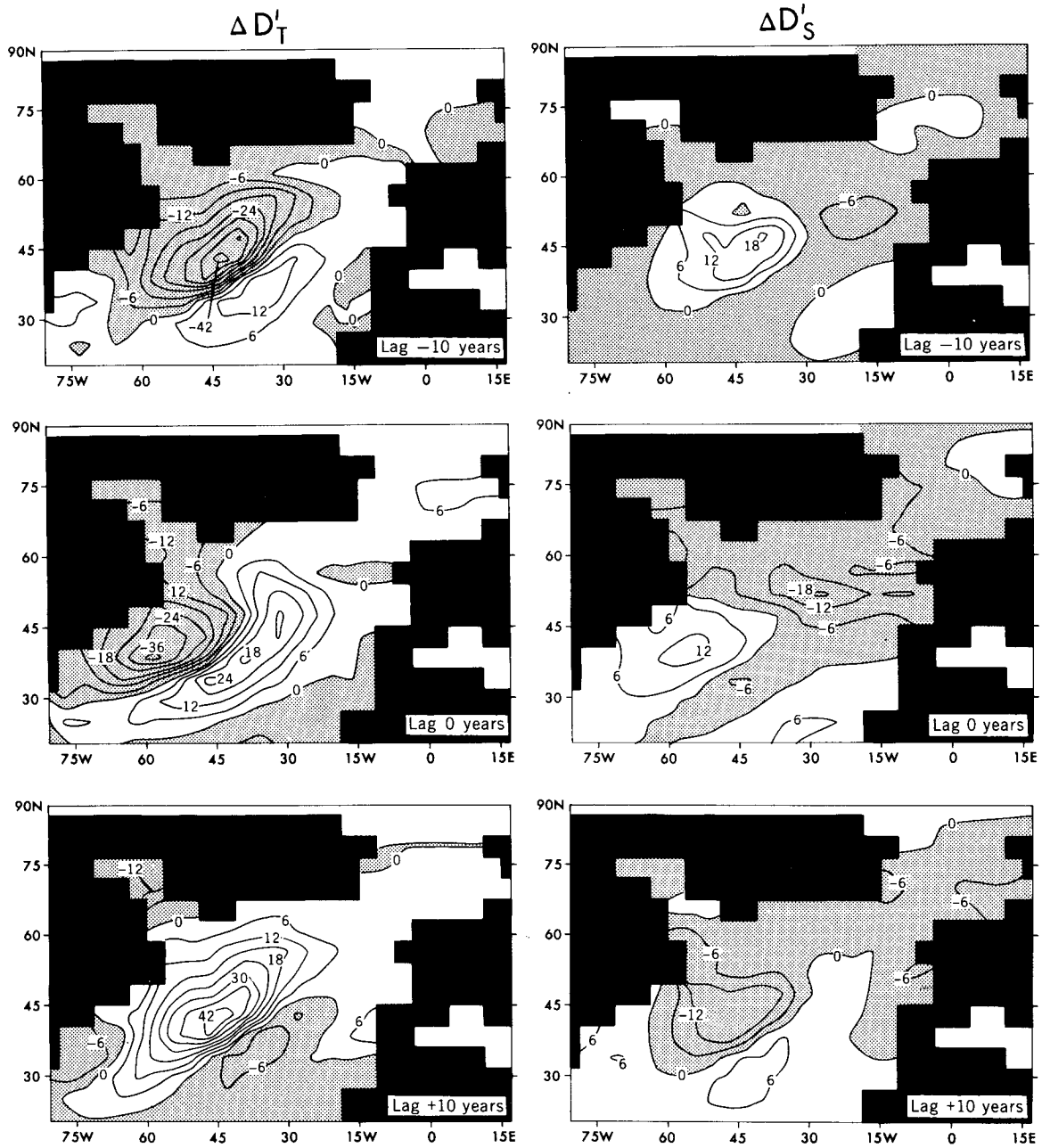

FIG. 19. Decomposition of the regression coefficients between dynamic topography and the THC into salinity- and temperature-induced components. The top row depicts regressions for lag − 10 years, the middle row depicts regressions for lag 0 years, the bottom row depicts regressions for lag + 10 years. Units are 10^2 cm^2 s^{-2}. Values less than zero are stippled. Left column: temperature-induced component of the regression coefficients between dynamic topography and the THC. Right column: salinity-induced component of the regression coefficients between dynamic topography and the THC.

the intensity of the THC. It is the interplay of these two circulations that appears to play a dominant role in the fluctuations of the THC. In order to illustrate this interrelationship, we can go through one "cycle" of a THC fluctuation. Since the starting point of an oscillation is arbitrary, we may begin with a weak THC (for example, conditions at lag −20 years). The reduced heat transport associated with this weak THC results in the development of a cold, dense pool throughout the top 1 km in the middle of the North Atlantic (see Fig. 18). This cold, dense pool has an associated cyclonic circulation, and corresponds approximately to

the conditions around lag −10 years. The anomalous flow across the mean salinity contours (see Fig. 1 for the mean salinity field) associated with this gyre circulation results in enhanced salt transport into the sinking region (see Fig. 17), thereby increasing the salinity and density of the sinking region. This process is associated with a strengthening of the THC until it reaches its maximum at lag 0 years. The result of this strengthening of the THC is that the northward advection of heat is enhanced, thereby generating a pool of warm, less dense water throughout the top 1 km in the middle of the North Atlantic (see Figs. 18 and 19). As this warm pool develops (lags 0 through +10 years), an anticyclonic gyre circulation is created, which acts to decrease the salt transport into the sinking region (see Fig. 17), thereby reducing density in the sinking region and weakening the THC. As the THC weakens, the heat transport is reduced, thereby generating once more a cold, dense pool in the North Atlantic. Thus, we have completed one "cycle."

The picture thus painted is rather conceptual, but provides an approximate fit to the available model evidence. What is clear in the model is the following: 1) density in the sinking region slightly precedes the intensity of the THC, 2) density in the sinking region is primarily controlled by salinity, 3) the transport of salt into the sinking region by the horizontal gyre circulation is critical in establishing the phase dependence of the density in the sinking region, and 4) the gyre circulation is primarily controlled by temperature-induced density anomalies throughout the top 1 km. From the above analyses the importance of the phase difference between vertically averaged temperature and salinity becomes apparent. Salinity-induced anomalies in the sinking region appear to drive the THC, and should thus have a phase quite similar to the THC. The primary effect of the temperature anomalies, however, is to generate the gyre circulation, which is out of phase with the THC. Note that it was shown in Fig. 11 that the maximum zonally averaged temperature anomalies are distinctly to the south of the maximum salinity anomalies. These temperature anomalies are the northern extent of the temperature anomalies responsible for the gyre circulations (see Fig. 19). Thus, the phase relationship between vertically averaged temperature and salinity is necessary for the gyre circulation to be in quadrature with the THC, which in turn appears to be important to the fluctuations.

While the above description of the temperature-induced gyre circulation is consistent with a stationary gyre, there is model evidence that this gyre circulation slowly propagates to the west with a speed on the order of $\sim$0.5–1 cm s^{-1}. This propagation is an interesting feature, although its relevance to the fluctuations of the THC is not clear.

The above discussion of a mechanism for these irregular oscillations relies principally on ocean processes, suggesting that the model phenomenon is primarily an oceanic feature. While there is some potential that low-frequency variations in the surface water fluxes may play a role, the analyses presented here suggest that they are secondary in importance to the oceanic transport processes in terms of the vertically averaged salt budget for the sinking region. However, anomalous surface water fluxes may still play a role by altering the vertical stability of the water column in the near-surface layer of the sinking region. This speculation is a subject for further investigation.

In addition to temperature and salinity, there are also variations in the surface winds over the North Atlantic accompanying the fluctuations of the THC. The anomalous low-level wind fields associated with the THC can be inferred from Fig. 20 in which regressions between surface pressure and the THC are shown. At lag 0 the anomalous geostrophic flow provides enhanced westerlies across the Atlantic from approximately 50°N to 65°N, thereby tending to increase the surface heat flux. At lag 20 the anomalous surface pressure field tends to decrease the near-surface westerlies. The phase of the surface pressure and wind variations is similar to the phase of the surface heat flux shown in Fig. 14 (the anomalous westerlies at lag 0 increase the flux of heat from the ocean to the atmosphere, corresponding to negative values in Fig. 14). This anomalous atmospheric flow is not confined to the near-surface layer, but extends well into the midtroposphere. The relative importance of these circulation changes to the mechanism of the irregular oscillation is not clear. Further, these changes in atmospheric pressure are not in agreement with the observational analyses of Kushnir (1993).

It is not anticipated that the variations in surface wind stress have a direct effect on the deep overturning circulation. Wind-driven cells of meridional circulation are shallow and do not substantially affect the deep thermohaline overturning of the Atlantic Ocean with the exception of the Circumpolar Ocean of the Southern Hemisphere. In that region, a wind-driven cell penetrates deeply due to the absence of a continental barrier that blocks the zonal current (Toggweiler and Samuels 1993). The primary effect of wind variations over the North Atlantic associated with the THC appears to be on the surface heat flux.

While the above suggested mechanism for these fluctuations in the intensity of the THC provides a fit to the available model evidence, additional analyses and experiments are needed to assess how robust such processes are. Among other issues, it is possible that the coarse spatial resolution in this model may affect the inherent temporal variability of the model. The dependence of this fluctuation on the choice of physical parameterizations is another issue to examine. Further, the role of the atmosphere in such low-frequency variability needs to be more thoroughly examined, particularly with regard to the surface freshwater flux.

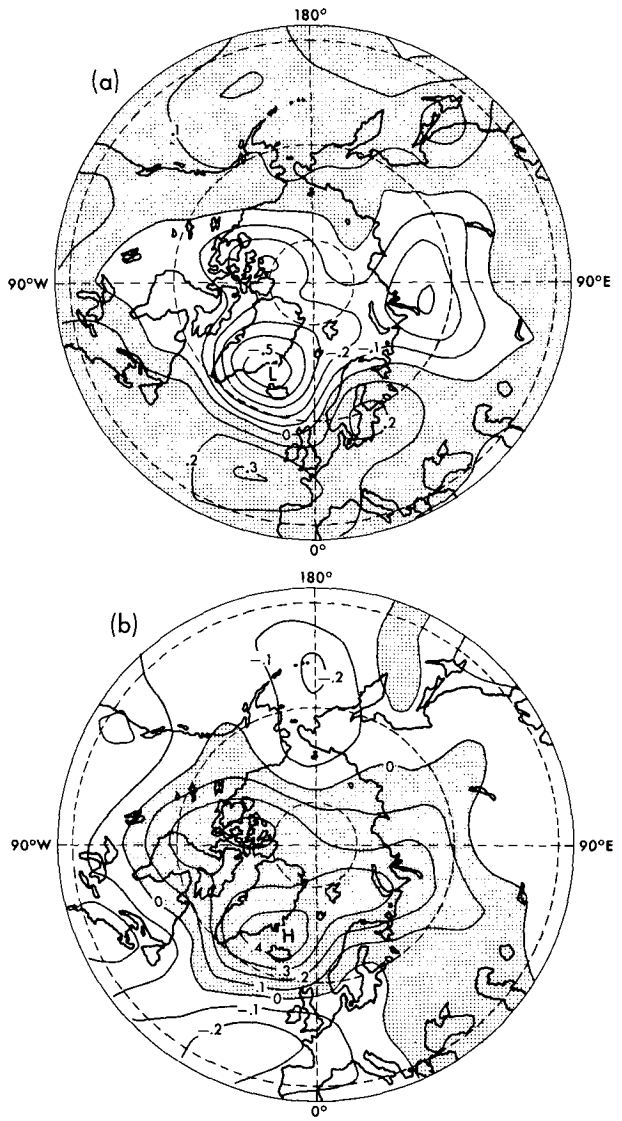

FIG. 20. Regression coefficients between surface pressure and the THC. Units are mb. (a) Lag 0 years. (b) Lag + 20 years.

4. Summary and discussion

It has been shown that an irregular oscillation of the thermohaline circulation (THC) in the North Atlantic Ocean appears in a coupled ocean–atmosphere model. This oscillation has a broad time scale of around 50 years, and appears to be driven by density anomalies in the sinking region of the North Atlantic Ocean combined with much smaller density anomalies of opposite sign in the broad, rising region. These density variations are in turn induced by fluctuations of the THC itself, as well as by transports of heat and salt associated with a horizontal gyre circulation. The transports accomplished by this gyre circulation appear to play a prominent role in the heat and salt anomalies associated with fluctuations in the THC. The analyses presented here suggest that the irregular oscillations in the THC intensity are primarily a result of oceanic processes, although the role of the atmosphere should be explored further. While it has not been confirmed here, one can speculate that the irregular oscillation is triggered by nearly random surface buoyancy forcing of heat and water fluxes.

Sea surface temperature fluctuations associated with the variations in the THC have a spatial pattern that bears encouraging resemblance to a pattern of observed interdecadal variability (Kushnir 1993). The sea surface temperature anomalies induce surface air temperature anomalies of substantial magnitude over the North Atlantic, northern Europe, and the Arctic. The interdecadal time scale of this variability points out the potential difficulty of distinguishing natural variability of the coupled climate system from anthropogenic climate change, which would be expected to occur on similar time scales.

Bjerknes (1964) suggested that low-frequency changes in SST over the northern North Atlantic are associated with variations in the intensity of the thermohaline circulation. The coupled model simulation illustrates a physically plausible mechanism for such a complex low-frequency air–sea interaction. All that can be concluded is that the model variability is broadly consistent with what little evidence is available. Future studies of both the instrumental record and proxy paleoclimatic data have the potential of producing new evidence to further constrain conceptual models of North Atlantic climate variability.

APPENDIX

Heat and Salt (Freshwater) Budgets

The mechanism of this irregular oscillation can be better understood by a consideration of the heat and salt (freshwater) budgets over the sinking region. As defined in the main text, the sinking region of the THC in the North Atlantic Ocean extends from 52°N to 72°N, from the North American coast to the European coast, and from the surface of the ocean to the bottom. This volume incorporates the vast majority of the sinking motion of the THC (see Fig. 3). The boundaries of the sinking region were shown schematically in Fig. 13. The budgets of heat and salt (fresh water) for this volume are evaluated based upon the following equation:

$$\frac{\partial}{\partial t}\int_{\lambda_1}^{\lambda_2}\left\{\int_{\theta_1}^{\theta_2}\left[\int_{z_b}^{0}\begin{pmatrix}CT\\S\end{pmatrix}\rho dz\right]a^2\cos\theta d\theta\right\}d\lambda$$

$$=\int_{\lambda_1(\theta_1)}^{\lambda_2(\theta_1)}\left[\int_{z_b(\theta_1,\lambda)}^{0}v\begin{pmatrix}CT\\S\end{pmatrix}\rho dz\right]a\cos\theta d\lambda$$

$$-\int_{\lambda_1(\theta_2)}^{\lambda_2(\theta_2)}\left[\int_{z_b(\theta_2,\lambda)}^{0}v\begin{pmatrix}CT\\S\end{pmatrix}\rho dz\right]a\cos\theta d\lambda+\int_{\lambda_1}^{\lambda_2}\int_{\theta_1}^{\theta_2}$$

$$\times \begin{pmatrix} \text{NDSR} - \text{NULR} - \text{SH} - \text{LH} \\ \bar{S}\cdot(E - P - r) \end{pmatrix} a^2 \cos\theta d\lambda$$

where t is time, v is meridional velocity, λ is longitude, θ is latitude, z is depth, θ_1 = latitude of southern boundary, θ_2 = latitude of northern boundary, λ_1, λ_2 = longitudinal boundaries of sinking region, z_b = depth of ocean (varies with latitude and longitude), a = radius of earth, P = precipitation, E = evaporation, r = runoff, S = salinity, T = temperature, ρ = density, C = specific heat for water, NDSR = net downward solar radiation, NULR = net upward longwave radiation, SH = sensible heat flux, and LH = latent heat flux.

The first and second terms on the right-hand side (rhs) of the equation represent the contributions from the northward transport of heat or salt at the southern and northern boundaries, respectively. The third term on the rhs represents the contributions from the surface fluxes of heat or fresh water. The sum of the three terms on the rhs is equal to the rate of change of the total heat or salt content in the sinking region, and is given by the left-hand side of the equation. Although contributions from subgrid-scale processes are neglected in this analysis, the computed budgets do achieve an approximate balance, both in the time mean and in their variations. The budget components are computed from monthly means. While the time averaging removes higher-frequency components in the budget terms, we are primarily interested in the lower frequencies.

The physical meaning of salt transport in the present model requires some explanation (Bryan 1969). The rigid-lid surface boundary condition requires that the vertical component of velocity is zero at the surface of the model ocean. Thus, an excess of rainfall over evaporation at the surface is considered a sink of salinity. Therefore, a net poleward transport of salt would be present when the excess of precipitation over evaporation in high latitudes is exactly compensated by the net equatorward transport of fresh water.

The horizontal transports were divided by the total surface area over the sinking region in order to facilitate comparison between the horizontal transport terms and the surface flux terms, such that both horizontal transport and surface flux terms have the same units. (In the computation of the heat transport the dependence of the specific heat on pressure, temperature, and salinity was neglected—the neglect of this factor should not appreciably affect the results.) The surface fluxes of heat and fresh water across the air–sea interface were also computed and spatially averaged over the sinking region.

In order to characterize the variations of these budget terms with respect to fluctuations in the THC, linear regressions were computed between the time series of various budget terms and the THC. Prior to the regression analyses, all time series were first detrended and filtered such that fluctuations with a time scale of less than approximately 10 years were effectively removed. The results of these regression analyses were shown in Figs. 14 and 15, and their implications for the temporal variations of temperature and salinity in the sinking region were discussed in the main text. In addition, the phase difference between the heat and salt transports, whereby the salt transport leads the heat transport, was also discussed in the main text.

Acknowledgments. The authors are very grateful to Kirk Bryan for his many valuable suggestions and interactions. Keith Dixon made numerous significant contributions, not only toward the detailed analysis of the model output, but also in diagnosing and correcting a critical numerical instability in a previous model integration. Our deep appreciation is extended to the director of GFDL, Jerry Mahlman, both for his support of this project and for insightful comments on a preliminary version of this manuscript. Isaac Held, Tony Broccoli, Robbie Toggweiler, Yochanan Kushnir, and Gabriel Lau, along with two anonymous reviewers, provided comments that were very useful in the improvement of this manuscript.

REFERENCES

Bjerknes, J., 1964: Atlantic air-sea interaction. *Adv. Geophys.*, **10**, 1–82.

Bloomfield, P., 1976: *Fourier Analysis of Time Series: An Introduction.* Wiley, 258 pp.

Bryan, K., 1969: Climate and the ocean circulation: III. The ocean model. *Mon. Wea. Rev.*, **97**, 806–827.

——, 1987: Potential vorticity in models of the ocean circulation. *Quart. J. Roy. Meteor. Soc.*, **113**, 713–734.

——, and L. J. Lewis, 1979: A water mass model of the world ocean. *J. Geophys. Res.*, **84**(C5), 2503–2517.

Chatfield, C., 1989: *The Analysis of Time Series: An Introduction.* Chapman and Hall, 241 pp.

Frankignoul, C., and K. Hasselmann, 1977: Stochastic climate models. Part II, Application to sea-surface temperature anomalies and thermocline variability. *Tellus*, **29**, 289–305.

Gordon, A. L., S. E. Zebiak, and K. Bryan, 1992: Climate variability and the Atlantic Ocean. *EOS*, **73**, 161–165.

Gordon, C. T., and W. Stern, 1982: A description of the GFDL global spectral model. *Mon. Wea. Rev.*, **110**, 625–644.

Kushnir, Y., 1993: Interdecadal variations in North Atlantic sea surface temperature and associated atmospheric conditions. *J. Climate*, submitted.

Levitus, S., 1989: Interpentadal variability of temperature and salinity at intermediate depths of the North Atlantic Ocean, 1970–1974 versus 1955–1959. *J. Geophys. Res.*, **94**(C5), 6091–6131.

Manabe, S., and R. J. Stouffer, 1988: Two stable equilibria of a coupled ocean–atmosphere model. *J. Climate*, **1**, 841–866.

——, ——, M. J. Spelman, and K. Bryan, 1991: Transient response of a coupled ocean–atmosphere model to gradual changes of atmospheric CO_2. Part I: Annual mean response. *J. Climate*, **4**, 785–818.

——, M. J. Spelman, and R. J. Stouffer, 1992: Transient response of a coupled ocean–atmosphere model to gradual changes of atmospheric CO_2. Part II: Seasonal response. *J. Climate*, **5**, 105–126.

Mikolajewicz, U., and E. Maier-Reimer, 1990: Internal secular variability in an ocean general circulation model. *Climate Dyn.*, **4**, 145–156.

Orszag, S. A., 1970: Transform methods for calculating vector-coupled sums: Application to the spectral form of the vorticity equation. *J. Atmos. Sci.*, **27**, 890–895.

Stouffer, R. J., S. Manabe, and K. Bryan, 1989: Interhemispheric asymmetry in climate response to a gradual increase of atmospheric CO_2. *Nature,* **342,** 660–662.

Toggweiler, J. R., and B. Samuels, 1993: Is the magnitude of deep outflow from the Atlantic Ocean actually governed by Southern Hemisphere wind? *The Global Carbon Cycle,* M. Heiman Ed., NATO ASI Series, Springer-Verlag, in press.

Weaver, A. J., and E. S. Sarachik, 1991: Evidence for decadal variability in an ocean general circulation model: An advective mechanism. *Atmos.-Ocean,* **29,** 197–231.

——, ——, and J. Marotzke, 1991: Internal low frequency variability of the ocean's thermohaline circulation. *Nature,* **353,** 836–838.

——, J. Marotzke, P. F. Cummins, and E. S. Sarachik, 1993: Stability and variability of the thermohaline circulation. *J. Phys. Oceanogr.,* **23,** 39–60.